

Observation of a Zero-Field Josephson Diode Effect in a Helimagnet Josephson Junction

Alexander Beach,¹ Mostafa Tanhayi Ahari,² Younghyuk Kim,³ Kannan Lu, Gregory MacDougall,¹ Matthew Gilbert,⁴ and Nadya Mason⁵

¹*Department of Physics and Materials Research Laboratory,
University of Illinois Urbana-Champaign, United States*

²*Department of Natural Sciences and Math, Transylvania University, United States*

³*Department of Mechanical Science & Engineering,
University of Illinois Urbana-Champaign, United States*

⁴*Department of Electrical & Computer Engineering,
University of Illinois Urbana-Champaign, United States*

⁵*Pritzker School of Molecular Engineering, University of Chicago, United States*

(Dated: December 2, 2025)

$\text{Cr}_{1/3}\text{NbS}_2$ is a transition metal dichalcogenide that is also a chiral helimagnet, and so lacks inversion symmetry and has non-zero Berry curvature in position and momentum space. It is well known that the combination of broken time-reversal symmetry and broken inversion symmetry can generate non-reciprocal phenomena, but the interplay between these kinds of systems and superconductivity is not well known. We present Josephson junctions fabricated from $\text{Cr}_{1/3}\text{NbS}_2$ that give magnetic diffraction patterns with asymmetry in both the magnetic field and the critical current. The non-reciprocity in positive critical current and negative critical current, generally called the Josephson diode effect, has an efficiency of up to $\eta = 20\%$ in some parts of the magnetic diffraction pattern and persists even at zero applied field. We propose that pinned Abrikosov vortices are a main mechanism for the asymmetric magnetic field response in this system, and that the non-zero spin chirality of the $\text{Cr}_{1/3}\text{NbS}_2$ causes the diode effect. Simulations of magnetic diffraction patterns from Josephson junctions with vortices present show offsets from zero-field consistent with observations, while simulations of chiral spin structures with an out-of-plane canting show a diode effect.

I. INTRODUCTION

The majority of experiments on non-reciprocal superconductivity focus on systems with strong spin-orbit coupling, conventional ferromagnetism, and external magnetic fields. However, the combination of proximity superconductivity with complex magnetic textures that host rich physics, such as antiferromagnets or altermagnets remains relatively unexplored. In this manuscript we present transport measurements of Josephson junctions fabricated with the chiral helimagnet $\text{Cr}_{1/3}\text{NbS}_2$. Compared to ferromagnets and antiferromagnets, $\text{Cr}_{1/3}\text{NbS}_2$ has a complex, non-collinear spin texture, after undergoing a magnetic phase transition at around 128 K. Above the transition it is paramagnetic, and below the transition the spin configuration becomes helimagnetic, with the helical axis pointing in the c -direction of the crystal shown in Figure 1a, with a helical period of 48 nm.[1] When an applied magnetic field is parallel to the helical axis, then the helimagnetic spin texture can become a chiral conical configuration, where the spins are canted along the helical axis. However, a magnetic field applied perpendicular to the helical axis (i.e. within the ab -plane of the crystal) can give rise to one-dimensional solitons.[2] $\text{Cr}_{1/3}\text{NbS}_2$ is also

a transition metal dichalcogenide, made of NbS_2 layers with intercalated Cr atoms in between the layers, and belongs to the space group $P6_322$. [1]

The simultaneous broken inversion symmetry and broken time-reversal symmetry in $\text{Cr}_{1/3}\text{NbS}_2$, along with its rich magnetic phase diagram, make it a good material for studying non-reciprocal effects. We observe that the $\text{Cr}_{1/3}\text{NbS}_2$ Josephson junctions exhibit the Josephson diode effect, and that magnetic diffraction patterns from the junctions show an offset from zero magnetic field and non-monotonic amplitude decay. We propose that the helimagnetic spin-texture of the $\text{Cr}_{1/3}\text{NbS}_2$ creates the diode effect, based on simulations done with helical spin textures. At the same time we propose that Abrikosov vortices in the leads of the junction are the cause of the offsets in magnetic field and unconventional magnetic diffraction patterns. Importantly, the simulated diode effect only occurs when the spins have some out-of-plane canting, i.e. when there is a chiral-conical configuration. To explain both the offset and the diode effect, we further suggest that there is an out-of-plane field from the $\text{Cr}_{1/3}\text{NbS}_2$ that creates vortices in the leads of the junctions, possibly do to finite thickness of the $\text{Cr}_{1/3}\text{NbS}_2$ flake compared to its helical period.

The interplay between broken time reversal and

spatial inversion symmetry, leading to non-reciprocal effects, was first deliberately observed in chiral molecules in an applied magnetic field, where it was found that the refractive index of the molecules depended on their handedness.[3] The class of known non-reciprocal effects arising from broken time reversal and inversion symmetries is now quite large, with the effects arising from chiral broken inversion symmetry often called magnetochiral anisotropies.[4–9] This has also come to include non-reciprocal charge transport in superconducting systems, prototypically thought of as the combination of a non-centrosymmetric superconductor with an applied magnetic field that breaks TRS.[10–12] In these systems it is possible for a supercurrent to flow in one direction, but in the opposite direction the current flow will be normal. In other words, the magnitudes of the positive and negative critical currents are not the same, $I_{c+} \neq I_{c-}$. [13] This phenomenon is generally called the superconducting diode effect, and often the Josephson diode effect, if the system is a Josephson junction.

Asymmetric critical current was observed as early as 1967, in wide, high current Josephson junctions made of tin films.[14] Schemes have also existed for producing a non-reciprocal supercurrent using arrays of Josephson junctions, long Josephson junctions, and intentionally designed fluxonic diodes.[15–18] There are also now examples of asymmetric critical currents in systems without explicitly broken time-reversal symmetry, such as strained heterostructures and electrically polarized materials.[19, 20] More recently though, the superconducting diode effect has been observed in materials where the nonreciprocity arises from intrinsic material properties, rather than as a consequence of circuit design.

In superconductor/ferromagnet bilayers the diode effect has been attributed to asymmetric vortex dynamics arising from the stray field of the ferromagnetic layer.[21] The Josephson diode effect under zero-field has been reported in non-centrosymmetric NbSe₂/Nb₃Br₈/NbSe₂ Josephson junctions and also in inversion-symmetric twisted tri-layer graphene.[22, 23] In the former case the diode effect is attributed to polarization of the junction inducing asymmetric Josephson tunneling, while in the latter case the diode effect is suspected to come from a spin polarization or polarization of the valley occupations. The diode effect has also been observed in atomic Josephson junctions with a magnetic impurity, where it is attributed to dissipation caused by quasiparticle currents that have a particle-hole asymmetry.[24] To date there is no universal explanation for the superconducting diode effect in all systems, as the exact

mechanism can be system specific.

II. EXPERIMENT

The Cr_{1/3}NbS₂ used in these experiments was grown via chemical vapor transport with an iodine transport gas, which resulted in plate-like hexagonal crystals of about 2 mm on a side. Representative crystals were characterized via single crystal x-ray diffraction and Laue diffraction. Analysis of the diffraction data confirmed the P6₃22 space group with Cr³⁺ atoms at the 2c site, consistent with the expected chiral structure, pictured in Figure 1a. Magnetization was measured using a SQUID magnetometer with applied field in the *ab*-plane (parallel to the large face of the crystal). Figure 1b shows that the magnetization has field hysteresis at temperatures below T_N, with the width of the hysteresis increasing with decreasing temperature, while above the transition temperature the behavior is paramagnetic. Figure 1c shows a sudden increase in magnetic susceptibility with decreasing temperature, with a sharp maximum of 22×10^6 emu/Oe at T_N = 132 K. The magnetization hysteresis is caused by the formation of a soliton lattice, and the susceptibility peak is associated with the transition to a helical spin structure.[25, 26]

The junctions are fabricated from thin flakes of Cr_{1/3}NbS₂ on Si substrates with 500 nm oxides that were cleaned by oxygen reactive ion etching to enhance flake adherence. All successfully proximity-coupled flakes were under 40 nm thick and were identified via atomic force microscopy. Electron beam lithography was used to pattern the junctions with pseudo-four-point leads, shown in Figure 2a, with at least 60 nm of DC plasma sputtered NbTiN. The samples were cooled to mK temperatures in a dilution refrigerator with a 6:1:1 T vector magnet. Electrical measurements were done with a combination of an SR830 lock-in amplifier, Keithley 2400 voltage source, Keithley 6221 current source, DC-DAQ, and custom electronics.

An optical microscope image of one of the junctions without NbTiN is shown in Figure 2a, where the dimensions of this junction are roughly $0.4 \mu\text{m} \times 2.6 \mu\text{m} \times 20 \text{ nm}$. The \hat{x} - and \hat{y} -directions are in the *ab*-plane of the crystal, which is also the plane of the junction. \hat{x} is defined as parallel to the current running through the junction, the \hat{y} -direction is defined as perpendicular to that current, and the \hat{z} -direction is perpendicular to the plane of the junction and is equivalent to the *c*-direction of the Cr_{1/3}NbS₂. Figure 2b shows an initial superconducting transition for the NbTiN leads at around 10.7 K, with a zero

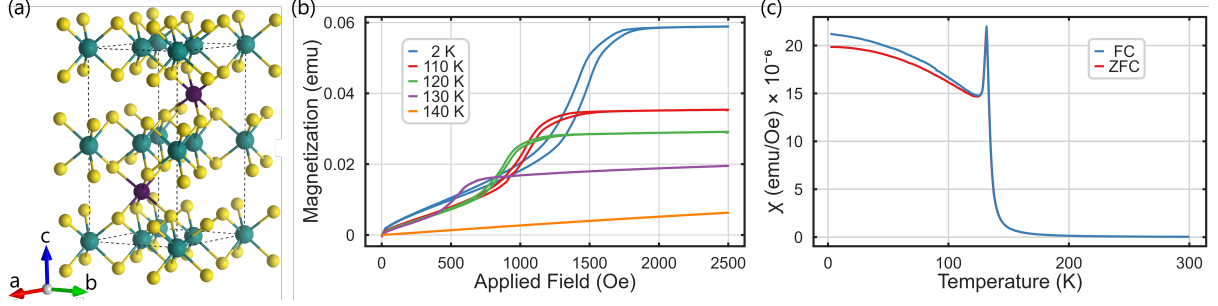


Figure 1. (a) The crystal structure of $\text{Cr}_{1/3}\text{NbS}_2$, Cr atoms (purple) are intercalated between the planes of NbS_2 (blue, yellow). (b) Applied magnetic field vs magnetization data showing magnetic hysteresis in bulk $\text{Cr}_{1/3}\text{NbS}_2$. Above the magnetic transition temperature there is a purely paramagnetic response. The hysteresis in the measurements below the transition temperature indicates the presence of solitons. (c) Magnetic susceptibility data for field-cooled and zero-field-cooled bulk $\text{Cr}_{1/3}\text{NbS}_2$, with a clear transition at ~ 132 K.

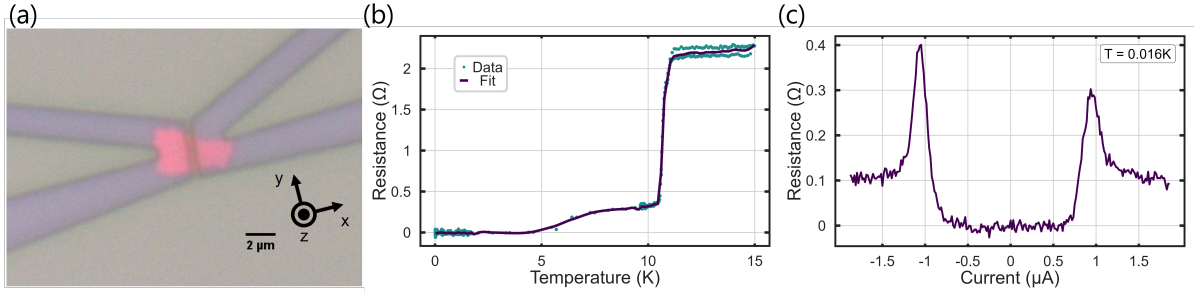


Figure 2. (a) An optical microscope image of a quasi-four-point Josephson junction, with a $\text{Cr}_{1/3}\text{NbS}_2$ weak link and NbTiN superconducting leads. (b) The resistance across the same junction as a function of temperature. The blue points are the raw data, and the red line is a fit. (c) The resistance of the junction as a function of applied current. This measurement was taken immediately after the initial cooldown to superconducting temperatures, with no applied magnetic field. There is a slight asymmetry in the positive and negative critical currents, as well as a difference in resistance peak amplitude at the critical currents.

resistance state below 4.6 K, and Figure 2c shows the critical current for the same junction at 16 mK with no applied magnetic field. The positive critical current is $0.94 \mu\text{A}$, while the negative critical current is $-1.05 \mu\text{A}$. These measurements indicate that the junction is well-proximitized and there is a zero-field Josephson diode effect, where the magnitude of the negative critical current is 12% larger than the positive critical current.

III. RESULTS

The magnetotransport measurements of the $\text{Cr}_{1/3}\text{NbS}_2$ junctions show several phenomena, including anomalous magnetic hysteresis, magnetic field asymmetry, magnetic field aperiodicity, and a diode effect. All of these phenomena result in magnetic diffraction pattern measurements that are significantly distorted from an ideal Fraunhofer pattern.

Figure 3 shows resistance measurements in the junction with out-of-plane magnetic field sweeps of varying magnitude and direction. In Figures 3a and 3b the magnetic field is swept from positive to negative, with the yellow curve starting at 0.05 T and the superconducting gap region shifted significantly from zero field. Darker curves start at smaller field magnitudes and are shifted less. There is a clear hysteresis in the critical field gap, with no sweep centered at zero magnetic field, and this is more apparent in Figure 3b where the magnetic field scale is logarithmic. The size of the critical field gap also increases with the strength of the starting field. The observed hysteretic behavior is not consistent with standard ferromagnetic hysteresis. In a weak ferromagnet a large positive field strongly magnetizes the material and simultaneously weakens superconductivity. As the magnetic field is brought towards zero, the remnant magnetization should continue to weaken superconductivity, and to return to an un-magnetized

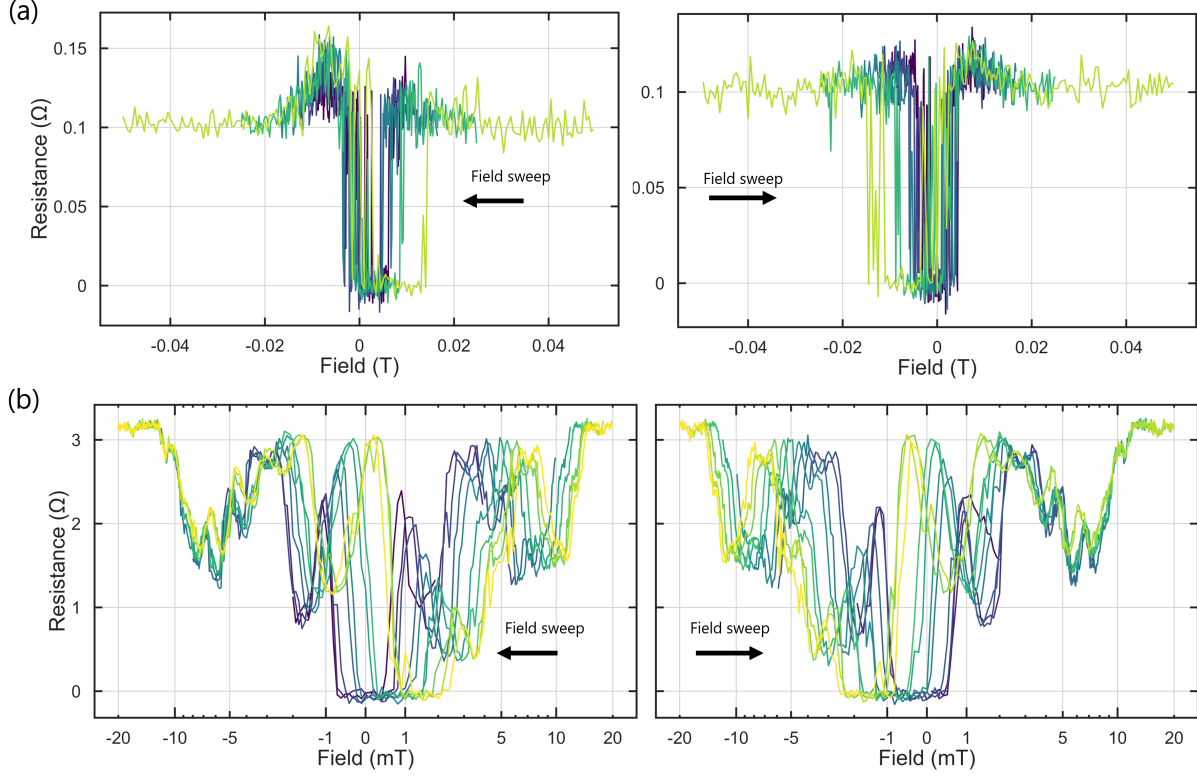


Figure 3. (a) The magnetoresistance of the junction as a magnetic field is applied perpendicular to the plane of the junction. The left plots show magnetic field sweeps going from positive magnetic field to negative magnetic field, and the right plots from negative to positive. The lighter yellow curves begin at larger field magnitudes and are further offset from zero, while the darker blue curves begin at smaller magnetic field values and show less hysteresis. (b) Magnetoresistance as a function of out-of-plane magnetic field strength for a second junction. The hysteresis is more apparent when plotted on a logarithmic scale, and multiple dips in resistance are seen at larger field values. The reproducibility of the curves suggests that the hysteresis and local extrema are part of the larger magnetic diffraction pattern.

state a small negative field must be applied to unpin the positive remnant magnetization, and so the proximitized superconductivity should be strongest (the critical current should be largest) at a small negative field. We report an opposite response, where a large positive (negative) magnetizing field does not need to be brought back to a negative (positive) field to recover a superconducting state; in fact a small positive (negative) field accomplishes this. Ferromagnetic Josephson junctions typically show either this expected behavior or negligible hysteresis.[28–30]

By applying a magnetic field and DC bias current together the magnetic hysteresis from Figure 3 presents as a magnetic diffraction pattern that is offset from zero field. Figure 4a shows that the nonstandard features appear in magnetic diffraction patterns with a field applied in the \hat{z} -direction, i.e. perpendicular to the applied current through the junction and parallel to the chiral axis of the $\text{Cr}_{1/3}\text{NbS}_2$.

Differential resistance measurements in Figures 4b and 4c show a clear diode effect for both positive and negative field, and that the direction of the effect does not depend on the sign of the magnetic field. The tilting of the lobes in Figure 4b shows that the diode efficiency of the effect varies with the magnetic field. Joule heating can mimic the Josephson diode effect, by asymmetrically changing critical current depending on the direction of the current sweep. This is ruled out as the cause of the observed diode effect in this manuscript for two reasons. First, the measured diode effect does not depend on the current sweep direction, whereas heating induced diode-like effects would. Second, the measured diode effect shows both a larger positive current magnitude and larger negative current magnitude without depending on the sign of the magnetic field and within the same measurement.

The magnetic diffraction patterns in Figure 5 show

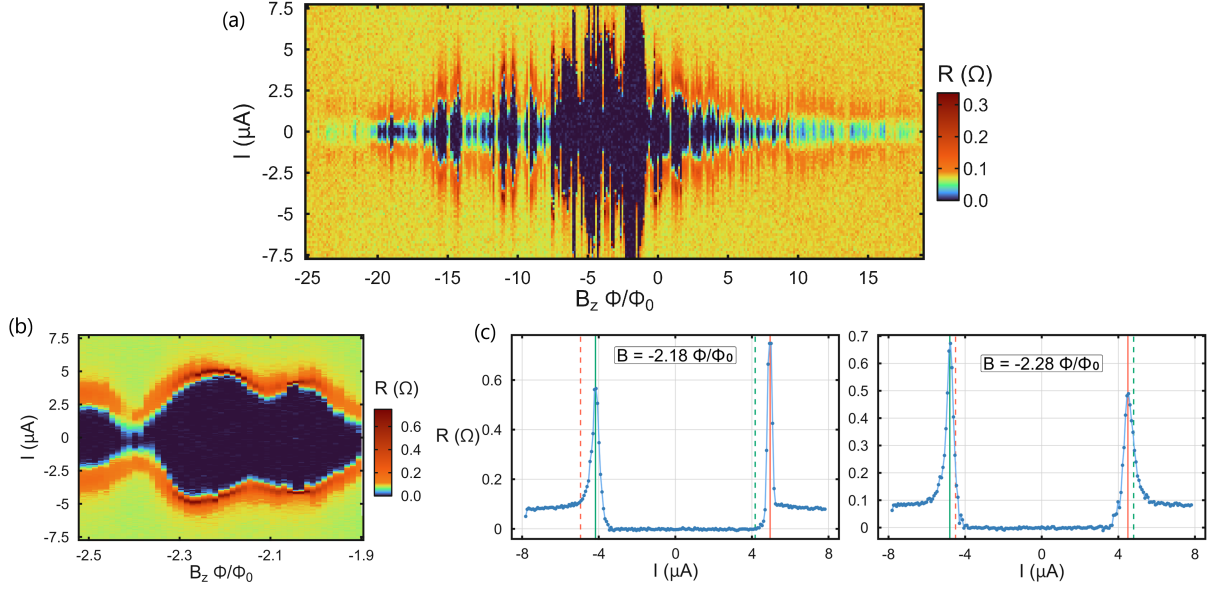


Figure 4. (a) Magnetic diffraction pattern in a $\text{Cr}_{1/3}\text{NbS}_2$ junction for a field applied perpendicular to the plane of the junction. The field has been normalized to units of flux divided by flux quanta using the cross-sectional area of the junction. There are several notable features: there is a shift of the patterns largest peak from zero magnetic field, a large asymmetry with respect to field, a decay in peak amplitude that does not follow the standard $\sin(\pi\Phi/\Phi_0)/(\pi\Phi/\Phi_0)$ Fraunhofer behavior, and a small diode effect. (b) A zoomed-in section of a magnetic diffraction measurement similar to a. In this section the superconducting diode effect is easily visible as a tilting of the lobes in the pattern. (c) Line cuts at specific flux values from b. The left image shows the diode effect with a larger magnitude positive critical current, while the right image shows a larger magnitude negative critical current. Note that both of these are at negative field values within a single flux quanta of each other.

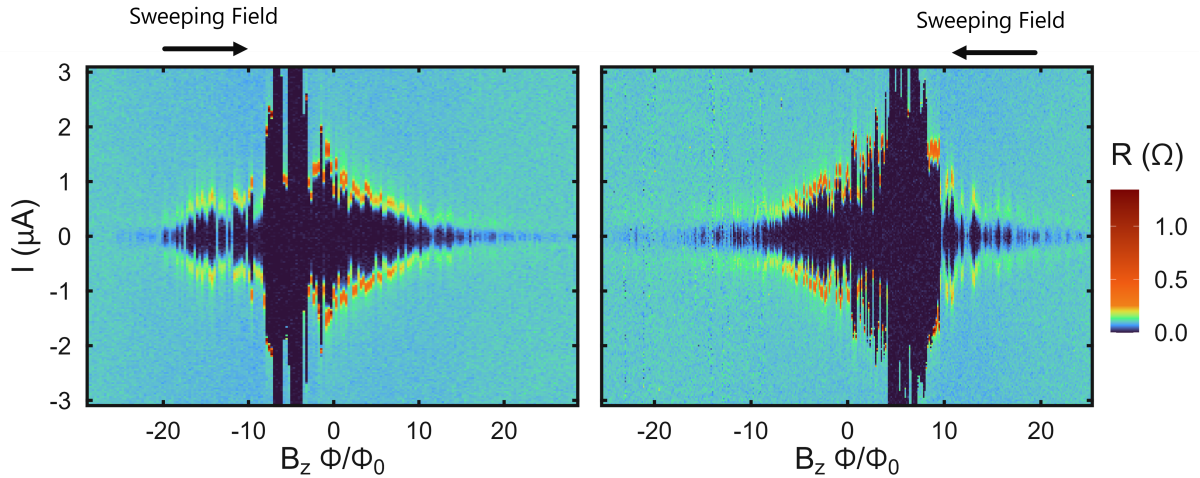


Figure 5. Magnetic diffraction patterns with a magnetic field sweeping from negative to positive, and positive to negative. The patterns are not perfect mirror images of each other, but do have the same overall shape and features. The central node shift away from zero field is not consistent with ferromagnetic hysteresis, where a positive (negative) coercive field is necessary to return from negative (positive) remnant magnetization to zero magnetization.[27]

multiple features that deviate from the standard $\sin(\pi\Phi/\Phi_0)/(\pi\Phi/\Phi_0)$ Fraunhofer behavior seen in rectangular SNS Josephson junctions. The node spacing of the patterns is aperiodic, rather than being spaced at integer flux quanta values. Note that the flux quanta values in the axes of Figure 5 are scaled from $\Phi = BA$, where B is the value of the applied magnetic field, and A is the actual cross-sectional area of the junction perpendicular to the field, and does not account for any flux focusing effects. In addition to aperiodicity the antinodal critical currents for larger applied fields do not monotonically decay, which can be seen clearly in Figure 5. Patterns with anomalous features have also been reported in other devices such as semiconductor Josephson junctions, topological insulator junctions, and ferromagnet junctions.[29, 31–33] It is known that asymmetry in magnetic diffraction patterns can be caused by slips in the superconducting phase difference across a junction and anisotropic magnetic susceptibility.[34] Such a phase skip can be caused by external magnetic fields or geometric defects in the junction. For junctions made from mechanically exfoliated materials if the junction is not rectangular or the height of the flake in the junction varies sharply, then the Rashba coefficient, which characterizes the strength of spin-orbit coupling, could vary across the junction. However, the junctions used in this experiment show no geometric defects in atomic force microscopy scans. Because we see these unconventional Fraunhofer features in multiple devices, with a coexisting Josephson diode effect, we lean towards more intrinsic material-specific mechanisms to explain these results. The next section will discuss the origin of the anomalous features in these helimagnet junctions, and reconcile them with the presence of the Josephson diode effect.

IV. ORIGINS OF THE DIODE EFFECT AND MAGNETIC ANOMALIES

We propose that a primary source of the magnetic field offsets in the magnetic diffraction patterns is the presence of Abrikosov vortices, and that the superconducting diode effect is primarily caused by the spin-chirality of the helimagnetic $\text{Cr}_{1/3}\text{NbS}_2$.

The vortices induce a phase difference in the junctions, through vortex currents and vortex fields, each dependent on the vortex core's proximity to the junction and the junction's geometry [35, 36]. For thick superconductor vortex currents circulating around the core decay with a characteristic length λ known as the London penetration length. In contrast, for a thin superconducting film $d \ll \lambda$, where d is the

thickness of the superconductor in the \hat{z} -direction, the characteristic length is given by the Pearl length $\lambda_P = \lambda^2/d$. When the vortex distance from the junction is comparable to the Pearl length, these currents cause a phase difference

$$\phi_v(y) = -V \arctan \frac{y - y_v}{|x_v|}, \quad (1)$$

across the junction. Here, (x_v, y_v) denotes the position of the vortex in the lead, and $V = +(-)1$ means the vorticity (antivortex). In contrast, when the vortex distance from the junction is larger than the Pearl length, the vortex current effects on the junction may be negligible. However, the vortex may have a long-range influence on the junction due to its stray magnetic fields [37]. These fields induce an effective magnetic flux within the junction, opposing the vortex's polarity. Due to flux-focusing effects in the junction region, this field can be significant, leading to a shift in the Fraunhofer pattern. Although the long-range vortex field and the short-range vortex circulating current are distinct effects, they can lead to a similar phase difference across the junction [37]. In the presence of a vortex, we obtain the magnetic interference pattern, i.e., the Fraunhofer pattern, as

$$I_{c+}(\Phi) = \max_{\phi} [I_{\text{tot}}(\phi, \Phi)], \quad (2)$$

$$I_{c-}(\Phi) = \min_{\phi} [I_{\text{tot}}(\phi, \Phi)], \quad (3)$$

where

$$I_{\text{tot}}(\phi, \Phi) = \frac{1}{L_y} \int_{-L_y/2}^{L_y/2} I_c \sin(\theta(y)) dy, \quad (4)$$

with a local phase, $\theta(y)$, defined as

$$\theta(y) = \phi + 2\pi \frac{\Phi}{\Phi_0} \frac{y}{L_y} + \phi_v(y). \quad (5)$$

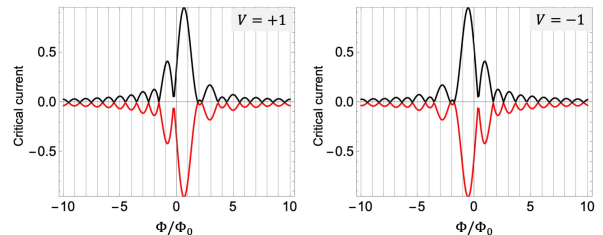


Figure 6. Fraunhofer patterns for vortex (left) and antivortex (right) at $(x_v, y_v) = (0.1, 0)$. Here, we set $L_y = \Phi_0 = 1$ and ignore the vortex stray fields, $\Phi_v = 0$.

Here, L_y is the lateral dimension of the junction perpendicular to the current direction and I_c is the critical current of the junction. Figure 6 shows the simulated Fraunhofer patterns for a (anti)vortex $V = (-) + 1$ at $(x_v, y_v) = (0.1, 0)$, with $L_y = I_c = 1$. Note that although $I_{c+}(\Phi) = |I_{c-}(\Phi)|$, the simulated Fraunhofer patterns show similar features to the measured Fraunhofer patterns, including: finite offsets from zero magnetic field, non-monotonic decay in the amplitude of the higher field lobes, and asymmetry about the central node. The phase difference given in Eq. (1) results in a central peak shift for the vortex and antivortex that are compatible with the exper-

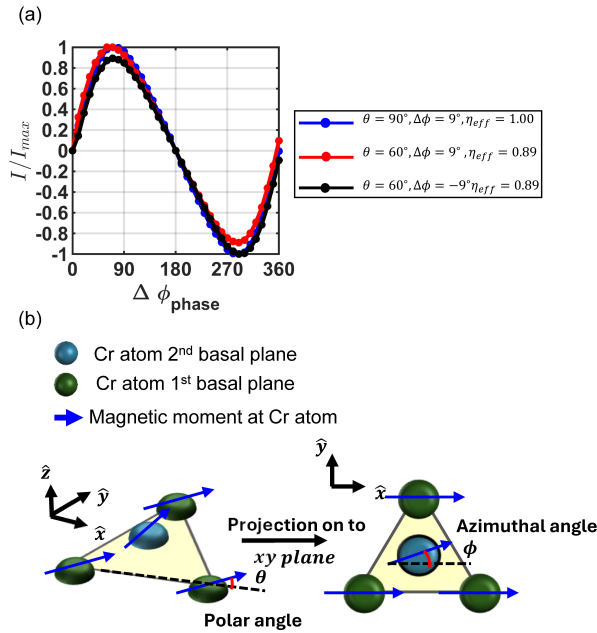


Figure 7. (a) Plot showing the normalized superconducting diode effect for different spin structures and corresponding diode efficiencies (η_{eff}), modeled using a two-part chiral and BCS Hamiltonian, shown in the Appendix. The data are normalized to I_{\max} . The blue line represents helical AFM phase ($\theta = 90^\circ$ and $\Delta\phi = 9^\circ$) with an efficiency of $\eta_{eff} = 1.00$. The red line represents conical spin structure ($\theta = 60^\circ$ and $\Delta\phi = 9^\circ$) with an efficiency of $\eta_{eff} = 0.89$. The black line represents chiral spin structure with opposite chirality ($\theta = 60^\circ$ and $\Delta\phi = -9^\circ$) with the same efficiency of $\eta_{eff} = 0.89$, but a reversed diode effect. (b) Diagram depicting the relative directions of the magnetic moments on Cr atoms in different planes. The polar angle, θ , is the in-plane rotation of the moment, while the azimuthal angle, ϕ , is the out-of-plane rotation of the moment. The diode effect only appears when there is an out-of-plane component to the moments, i.e. in the crystallographic c -direction of $\text{Cr}_{1/3}\text{NbS}_2$.

imental Fraunhofer patterns in Figure 5 (sweeping the field from a large positive field to zero and a large negative field to zero). Notably, if there were a ferromagnetic domain in the $\text{Cr}_{1/3}\text{NbS}_2$, it would also shift the Fraunhofer pattern. However, in our observations, the observed shift is attributed to the vortex-induced phase difference, evidenced by the critical current's maximum occurring before the magnetic field sweeps to zero, contrary to the behavior expected with a ferromagnetic domain. Considering the effect of vortex flux Φ_v would enhance the shift in the Fraunhofer patterns and agree with the magnetic behavior of the junction.

A key question is whether vortices are spontaneously created or explicitly nucleated by external magnetic fields. We suggest that the magnetization of the $\text{Cr}_{1/3}\text{NbS}_2$ is the source of the vortices in our devices, through a combination of a finite out-of-plane magnetic moment while the material is in a chiral conical spin configuration and stray fields from the edges of the exfoliated flake. Previous simulations have shown that in a superconductor/helimagnet bilayer system, where the chiral axis is in the plane of the superconductor, the helical magnetic field can induce vortices in the superconductor.[38] It has also been reported that vortex pinning at the edges of a superconducting film can produce a diode effect in superconducting thin-films.[39] These vortices could be caused by the fringing field at the edge of a neighboring ferromagnetic layer, or a small applied field fringing around a jagged edge of the superconducting film. Below the magnetic transition temperature, each layer of Cr atoms in $\text{Cr}_{1/3}\text{NbS}_2$ is akin to a ferromagnetic thin-film, and the edge of an exfoliated flake could have a complicated geometry. This field may also provide a Zeeman interaction, which combined with the spin-orbit coupling present in $\text{Cr}_{1/3}\text{NbS}_2$ could lead to a diode effect. Another explanation for the anomalous hysteresis and asymmetry in the magnetic diffraction patterns is the presence of chiral domain walls in the crystal. The dynamics of chiral domain walls with the application of a magnetic field can show similar effects to vortices.[40, 41]

While pinned Abrikosov vortices can explain the magnetic field shifts, aperiodicity, and non-monotonic decay in the magnetic diffraction patterns, they do not account for the Josephson diode effect by themselves. Rather, a combination of IS and TRS breaking are known to be able to induce the diode effect, which can be thought of as having Cooper pairs with finite-momentum coupling that carry directional supercurrent.[42, 43] Because of the symmetry breaking requirements, the diode effect typically appears with an external electric or magnetic field; however,

$\text{Cr}_{1/3}\text{NbS}_2$ can inherently satisfy the IS and TRS conditions because of its chiral spin structure. The $P6_322$ space group that $\text{Cr}_{1/3}\text{NbS}_2$ is non-centrosymmetric.

At the same time, the chiral spin structure induces effective spin-orbit coupling, breaking inversion symmetry. The bulk chiral helimagnetic structure of $\text{Cr}_{1/3}\text{NbS}_2$ is an antiferromagnetic phase that preserves TRS, but for crystal thicknesses below the chiral period of 48 nm, there is a net magnetic field. In both bulk and exfoliated crystals, the chiral conical spin structure also has a non-vanishing net moment, breaking TRS. Although the chiral conical structure is not the default state for spins in $\text{Cr}_{1/3}\text{NbS}_2$, it can be induced by a magnetic field. Additionally, strain is known to induce new magnetic phases in $\text{Cr}_{1/3}\text{NbS}_2$, which could be caused by the deposition the metallic leads or thermal stresses from cooling.[44] Non-centrosymmetric superconductors can also host spin-singlet and spin-triplet pairing in the presence of magnetic ordering, and there is evidence for spin-triplet pairing in superconductor/ $\text{Cr}_{1/3}\text{NbS}_2$ heterostructures, which can also lead to a diode effect.[45–48]

We focus on explaining the diode effect via the chiral conical phase of $\text{Cr}_{1/3}\text{NbS}_2$. To understand how the spin structure could induce the diode effect, we study the current-phase relationship in a Josephson junction with a chiral spin structure using a tight-binding and non-equilibrium Green’s function formulation. The crystal structure of the simulated junction is designed to preserve IS. The spin orientation is represented by $S_n = (\sin(\theta) \cos(n\phi), \sin(\theta) \sin(n\phi), \cos(\theta))$, where θ is the polar angle between the z -axis and the spin, ϕ is the azimuthal angle that rotates in the x - y plane, and n is the number of layers along the \hat{z} direction. We demonstrate in Figure A1 that the junction exhibits the diode effect when $\theta = \frac{\pi}{3}$, where the spin structure is in a chiral conical configuration. Conversely, the junction does not maintain the diode effect when $\theta = \frac{\pi}{2}$, where the spin structure is in a chiral helical antiferromagnetic configuration. Detailed results and the methodology for the supercurrent calculation are provided in the Appendix.

To summarize, the $\text{Cr}_{1/3}\text{NbS}_2$ Josephson junctions studied in this experiment show both a Josephson diode effect, and magnetic diffraction patterns with pronounced asymmetry and offsets from zero mag-

netic field. We suggest that the primary cause of the Fraunhofer anomalies is the presence of one or more Abrikosov vortices. The superconducting diode’s rectification direction does not depend directly on the direction of the applied field, unlike in devices where the diode’s directionality is switched by the direction of the applied field. This suggests a relation between the broken IS and broken TRS caused by the helimagnetism of the $\text{Cr}_{1/3}\text{NbS}_2$. Spins in helimagnets can form a chiral conical configuration, and simulations of a Josephson junction with such a chiral conical spin structure show a diode effect. Simulations of a Josephson junction with a phase difference caused by the addition of a single vortex or anti-vortex produce Fraunhofer patterns with an asymmetry about their central lobe, that are also offset from zero magnetic field. Both the chiral conical spin structure and presence of vortices can be caused by the presence of a magnetic field perpendicular to the plane of the junction. While some preliminary evidence suggests that the vortices are generated by the chiral field of the helimagnet, further studies are needed to disentangle intrinsic effects from potential external factors.

V. ACKNOWLEDGMENTS

This work was supported by NSF-BSF under DMR-2422090 and by the U.S. Department of Energy, Office of Science, National Quantum Information Science Research Centers. The experiment was carried out using some facilities of the Illinois MRSEC, supported by NSF DMR-1720633. X-ray diffraction measurements were taken in the George L. Clark X-ray Facility in the 3M Materials Chemistry Laboratory, at the University of Illinois Urbana-Champaign, while magnetization measurements were done in the University of Illinois Urbana-Champaign Materials Research Laboratory using a Quantum Design MPMS3 SQUID magnetometer. Laue diffraction measurements were taken also taken in the Materials Research Laboratory.

VI. DATA AVAILABILITY

All data supporting the findings in this study can be accessed via Reference [49].

-
- [2] Y. Cao, Z. Huang, Y. Yin, H. Xie, B. Liu, W. Wang, C. Zhu, D. Mandrus, L. Wang, and W. Huang, *Materials Today Advances* **7**, 100080 (2020).
 - [3] G. L. J. A. Rikken and E. Raupach, *Nature* **390**, 493 (1997).
 - [4] L. Barron and J. Vrbancich, *Molecular Physics* **51**, 715 (1984), <https://doi.org/10.1080/00268978400100481>.
 - [5] T. Ideue, K. Hamamoto, S. Koshikawa, M. Ezawa, S. Shimizu, Y. Kaneko, Y. Tokura, N. Nagaosa, and Y. Iwasa, *Nature Physics* **13**, 578 (2017).
 - [6] M. Atzori, C. Train, E. A. Hillard, N. Avarvari, and G. L. J. A. Rikken, *Chirality* **33**, 844 (2021), <https://onlinelibrary.wiley.com/doi/pdf/10.1002/chir.23361>.
 - [7] H. F. Legg, M. Rößler, F. Munning, D. Fan, O. Breunig, A. Bliesener, G. Lippertz, A. Uday, A. A. Taskin, D. Loss, J. Klinovaja, and Y. Ando, *Nature Nanotechnology* **17**, 696 (2022).
 - [8] G. L. Rikken and N. Avarvari, *The Journal of Physical Chemistry Letters* **14**, 9727–9731 (2023).
 - [9] F. Qin, W. Shi, T. Ideue, M. Yoshida, A. Zak, R. Tenne, T. Kikitsu, D. Inoue, D. Hashizume, and Y. Iwasa, *Nature Communications* **8**, 14465 (2017).
 - [10] N. Nunchot and Y. Yanase, *Phys. Rev. B* **109**, 054508 (2024).
 - [11] K. Misaki and N. Nagaosa, *Phys. Rev. B* **103**, 245302 (2021).
 - [12] L. Bauriedl, C. Bäuml, L. Fuchs, C. Baumgartner, N. Paulik, J. M. Bauer, K.-Q. Lin, J. M. Lupton, T. Taniguchi, K. Watanabe, C. Strunk, and N. Paradiso, *Nature Communications* **13**, 4266 (2022).
 - [13] M. Nadeem, M. S. Fuhrer, and X. Wang, Superconducting diode effect – fundamental concepts, material aspects, and device prospects (2023), arXiv:2301.13564 [cond-mat.supr-con].
 - [14] A. M. Goldman and P. J. Kreisman, *Phys. Rev.* **164**, 544 (1967).
 - [15] E. Trías, J. J. Mazo, F. Falo, and T. P. Orlando, *Phys. Rev. E* **61**, 2257 (2000).
 - [16] F. Falo, P. J. Martínez, J. J. Mazo, T. P. Orlando, K. Segall, and E. Trías, *Applied Physics A* **75**, 263 (2002).
 - [17] F. Raissi and J. Nordman, *IEEE Transactions on Applied Superconductivity* **5**, 2943 (1995).
 - [18] G. Carapella and G. Costabile, *Phys. Rev. Lett.* **87**, 077002 (2001).
 - [19] F. Liu, Y. M. Itahashi, S. Aoki, Y. Dong, Z. Wang, N. Ogawa, T. Ideue, and Y. Iwasa, *Science Advances* **10**, eado1502 (2024), <https://www.science.org/doi/pdf/10.1126/sciadv.ado1502>.
 - [20] Y. Zhang, Y. Gu, P. Li, J. Hu, and K. Jiang, *Phys. Rev. X* **12**, 041013 (2022).
 - [21] A. Gutfreund, H. Matsuki, V. Plastovets, A. Noah, L. Gorzawski, N. Fridman, G. Yang, A. Buzdin, O. Millo, J. W. A. Robinson, and Y. Anahory, *Nat Commun* **14**, 1630 (2023).
 - [22] H. Wu, Y. Wang, Y. Xu, P. K. Sivakumar, C. Pasco, U. Filippozzi, S. S. P. Parkin, Y.-J. Zeng, T. McQueen, and M. N. Ali, *Nature* **604**, 653 (2022).
 - [23] J.-X. Lin, P. Siriviboon, H. D. Scammell, S. Liu, D. Rhodes, K. Watanabe, T. Taniguchi, J. Hone, M. S. Scheurer, and J. Li, *Nature Physics* **18**, 1221–1227 (2022).
 - [24] M. Trahms, L. Melischek, J. F. Steiner, B. Mahendru, I. Tamir, N. Bogdanoff, O. Peters, G. Reecht, C. B. Winkelmann, F. von Oppen, and K. J. Franke, *Nature* **615**, 628 (2023).
 - [25] N. Sirica, P. Vilmercati, F. Bondino, I. Pis, S. Nappini, S.-K. Mo, A. V. Fedorov, P. K. Das, I. Vobornik, J. Fujii, L. Li, D. Sapkota, D. S. Parker, D. G. Mandrus, and N. Mannella, *Communications Physics* **3**, 65 (2020).
 - [26] E. M. Clements, R. Das, L. Li, P. J. Lampen-Kelley, M.-H. Phan, V. Keppens, D. Mandrus, and H. Srikanth, *Scientific Reports* **7**, 6545 (2017).
 - [27] N. O. Birge and N. Satchell, *APL Materials* **12**, 041105 (2024), https://pubs.aip.org/aip/apm/article-pdf/doi/10.1063/5.0195229/19866826/041105_1_5.0195229.pdf.
 - [28] I. Petković, M. Aprili, S. E. Barnes, F. Beuneu, and S. Maekawa, *Phys. Rev. B* **80**, 220502 (2009).
 - [29] L. Ai, E. Zhang, J. Yang, X. Xie, Y. Yang, Z. Jia, Y. Zhang, S. Liu, Z. Li, P. Leng, X. Cao, X. Sun, T. Zhang, X. Kou, Z. Han, F. Xiu, and S. Dong, *Nature Communications* **12**, 10.1038/s41467-021-26946-w (2021).
 - [30] G. Qiu, H.-Y. Yang, L. Hu, H. Zhang, C.-Y. Chen, Y. Lyu, C. Eckberg, P. Deng, S. Krylyuk, A. V. Davydov, R. Zhang, and K. L. Wang, *Nature Communications* **14**, 6691 (2023).
 - [31] H. J. Suominen, J. Danon, M. Kjaergaard, K. Flensberg, J. Shabani, C. J. Palmstrøm, F. Nichele, and C. M. Marcus, *Phys. Rev. B* **95**, 035307 (2017).
 - [32] W. Mayer, M. C. Dartiailh, J. Yuan, K. S. Wickramasinghe, E. Rossi, and J. Shabani, *Nature Communications* **11**, 212 (2020).
 - [33] A. Assouline, C. Feuillet-Palma, N. Bergeal, T. Zhang, A. Mottaghizadeh, A. Zimmers, E. Lhuillier, M. Eddrie, P. Atkinson, M. Aprili, and H. Aubin, *Nature Communications* **10**, 126 (2019).
 - [34] A. Beach, D. Reig-i Plessis, G. MacDougall, and N. Mason, *Journal of Physics: Condensed Matter* **33**, 425601 (2021).
 - [35] T. Golod, A. Rydh, and V. M. Krasnov, *Phys. Rev. Lett.* **104**, 227003 (2010).
 - [36] J. R. Clem, *Phys. Rev. B* **84**, 134502 (2011).
 - [37] T. Golod, A. Pagliero, and V. M. Krasnov, *Phys. Rev. B* **100**, 174511 (2019).
 - [38] S. Fukui, M. Kato, Y. Togawa, and O. Sato, *Journal of Physics: Conference Series* **1054**, 012027 (2018).

-
- [39] Y. Hou, F. Nichele, H. Chi, A. Lodesani, Y. Wu, M. F. Ritter, D. Z. Haxell, M. Davydova, S. Ilić, O. Glezakou-Elbert, A. Varambally, F. S. Bergeret, A. Kamra, L. Fu, P. A. Lee, and J. S. Moodera, *Phys. Rev. Lett.* **131**, 027001 (2023).
 - [40] F. Kidwingira, J. D. Strand, D. J. V. Harlingen, and Y. Maeno, *Science* **314**, 1267 (2006), <https://www.science.org/doi/pdf/10.1126/science.1133239>.
 - [41] A. Bouhon and M. Sigrist, *New Journal of Physics* **12**, 043031 (2010).
 - [42] M. Davydova, S. Prembabu, and L. Fu, *Science Advances* **8**, eabo0309 (2022), <https://www.science.org/doi/pdf/10.1126/sciadv.abo0309>.
 - [43] B. Pal, A. Chakraborty, P. K. Sivakumar, M. Davydova, A. K. Gopi, A. K. Pandeya, J. A. Krieger, Y. Zhang, M. Date, S. Ju, N. Yuan, N. B. M. Schröter, L. Fu, and S. S. P. Parkin, *Nature Physics* **18**, 1228 (2022).
 - [44] G. Paterson, A. Tereshchenko, S. Nakayama, Y. Kousaka, J. Kishine, S. McVitie, A. Ovchinnikov, I. Proskurin, and Y. Togawa, *Physical Review B* **101**, 184424 (2020).
 - [45] M. Yogi, Y. Kitaoka, S. Hashimoto, T. Yasuda, R. Settai, T. D. Matsuda, Y. Haga, Y. Ōnuki, P. Rogl, and E. Bauer, *Phys. Rev. Lett.* **93**, 027003 (2004).
 - [46] S. Yip, *Annual Review of Condensed Matter Physics* **5**, 15 (2014).
 - [47] A. Spuri, D. Nikolić, S. Chakraborty, M. Klang, H. Alpern, O. Millo, H. Steinberg, W. Belzig, E. Scheer, and A. Di Bernardo, *Phys. Rev. Res.* **6**, L012046 (2024).
 - [48] Y. Mao, Q. Yan, Y.-C. Zhuang, and Q.-F. Sun, *Phys. Rev. Lett.* **132**, 216001 (2024).
 - [49] Alexander Beach, *AlexanderBeach/observation-of-a-zero-field-Josephson-diode-effect-in-a-helimagnet-Josephson-junction: Observation of a zero-field josephson diode effect in a helimagnet josephson junction v1.0* (2025).
 - [50] Q.-f. Sun, J. Wang, and T.-h. Lin, *Physical Review B* **62**, 648 (2000).
 - [51] J. C. Cuevas, A. Martín-Rodero, and A. L. Yeyati, *Physical Review B* 10.1103/physrevb.54.7366 (1996), cond-mat/9605023.
 - [52] S. Ishizaka, J. Sone, and T. Ando, *Physical Review B* **52**, 10.1103/physrevb.52.8358 (1995).

MODELING THE CHIRAL SPIN STRUCTURE OF $\text{CR}_{1/3}\text{NBS}_2$

We begin our modeling by constructing the Hamiltonian as follows:

$$H_T = H_C + H_{BCS} \quad (\text{A1})$$

where H_C represents the middle part of the junction with a square lattice structure and chiral spin structure, and H_{BCS} denotes the left and right superconducting contacts of the junction. We project the sample onto the 2-dimensional \hat{x}, \hat{z} plane to account for the transport direction and helical axis. The dimensions are denoted as $N_x = 7$, $N_z = 11$. In real space, both terms of the Hamiltonian can be expressed as:

$$H_C = -t \sum_{i,j,\alpha} c_{i,j,\alpha}^\dagger c_{i+1,j,\alpha} - t \sum_{ij} c_{i,j,\alpha}^\dagger c_{i,j+1,\alpha} + \Delta_c \vec{\sigma} \cdot \hat{\mathbf{n}}_j \quad (\text{A2})$$

and

$$H_{BCS} = \sum_{ij,\alpha} \Delta_{i,j}^* c_{i,j,\uparrow}^\dagger c_{i,j,\downarrow}^\dagger + \Delta_{i,j} c_{i,j,\uparrow} c_{i,j,\downarrow}. \quad (\text{A3})$$

Here, $c_{i,j,\alpha} = (c_{i,j,\uparrow}, c_{i,j,\downarrow})^T$ are the creation and annihilation operators at the (i, j) -th atom of the square lattice in the \hat{x}, \hat{z} plane, α represents the spin degree of freedom, and $\vec{\sigma}$ are the Pauli matrices corresponding to the spin degrees of freedom. The final term accounts for the magnetism in the lattice manifest in the spin exchange between $\hat{\mathbf{n}}$ representing the magnetization, and Δ_c represents the intensity of the exchange. To account for the helical spin structure, $\hat{\mathbf{n}}_j = (\sin(\theta) \cos(j\phi), \sin(\theta) \sin(j\phi), \cos(\theta))$, where θ is polar angle, ϕ is azimuthal angle, and j is the number of layers along the \hat{z} -direction. $\Delta_{i,j}$ accounts for s-wave superconducting order parameter at (i, j) . To account for the semi-infinite superconducting contacts at the left ($x = 0$) and right ($x = 7$), we use the self-energy formalism in the Green's function as follows, [50–52],

$$G^R(\epsilon) = (\epsilon I + i\eta - H_T)^{-1} = (\epsilon I + i\eta - H_C - \Sigma_L - \Sigma_R)^{-1} \quad (\text{A4})$$

where

$$\Sigma_{L(R)}(\epsilon) = \frac{\tau_{L(R)}}{2} \beta(\epsilon) \times \begin{pmatrix} I & i \frac{\Delta_{L(R)}}{\epsilon} \sigma_y e^{i\phi_{L(R)}} \\ -i \frac{\Delta_{L(R)}}{\epsilon} \sigma_y e^{i\phi_{L(R)}} & I \end{pmatrix} \quad (\text{A5})$$

In this context, ϵ is the energy, I is the identity matrix for corresponding dimension, η is a small positive value for avoiding singularity in Green's function, $\tau_{L(R)}$ is the tunneling constant at left(right) contact, $\beta(\epsilon)$ is the ratio between the superconducting state and the normal density of state, σ_y is one of the Pauli matrices, $\Delta_L R$ is superconducting order parameter at the left (right) contact, and $\phi_{L(R)}$ is the superconducting phase at the left (right) contact.

In a Josephson junction, the superconducting order at the contact penetrates the middle part in order to lower the free energy. With the constructed Green's function, we utilize the self-consistent calculation to reach the ground state of the junction. The pairing superconducting potential is obtained from the energy spectrum of H_T and then fed back into H_T to calculate a new energy spectrum.

After the Hamiltonian reaches the ground state, we use the Green's function to obtain the supercurrent induced from Andreev reflection and the current-phase relationship (CPR) as follows:

$$I_{\text{supercurrent}} = \sum_{\mu,\nu,\alpha} \lambda \Gamma_{\nu,\alpha}^\mu G_{\nu,\alpha'}^\mu \quad \text{where} \quad \mu \in \{L, R\}, \nu \in \{h, e\}, \alpha(\alpha') \in \{\uparrow(\downarrow), \downarrow(\uparrow)\} \quad (\text{A6})$$

Here, μ is an index for electron (lesser) or hole (greater) electron degree of freedom, λ has a value of $1(-1)$ for electron(hole), ν is an index for left and right, α is the spin degree of freedom. These indices are

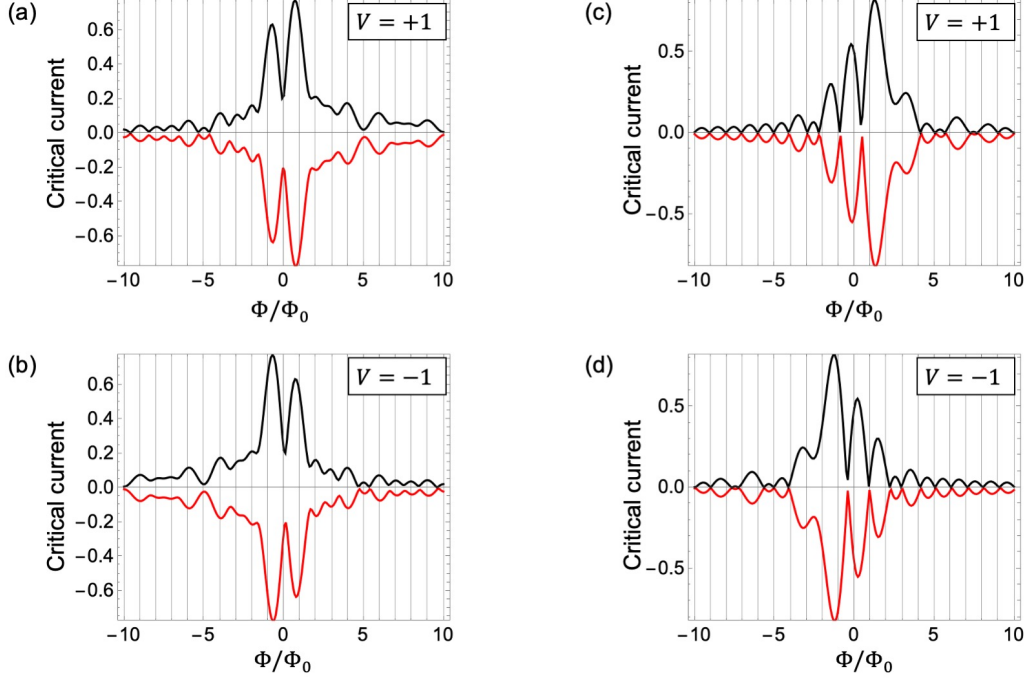


Figure A1. Fraunhofer patterns for a single vortex (a) antivortex (b) at $(x_v, y_v)/L_y = (0.01, 0.1)$, and double vortex (c) antivortex (d) at $(x_{v_1}, y_{v_1})/L_y = (0.05, 0.1)$, $(x_{v_2}, y_{v_2})/L_y = (0.05, -0.1)$.

used in the lesser and greater Green's functions, $G^\mu\nu, \alpha'$, and the broadening (linewidth) function, $\Gamma^\mu\nu, \alpha$. In supplementary Fig. 7 we show CPRs at $\theta = 60^\circ, 90^\circ$, which correspond to the conical or helical spin structures. The CPR shows the diode effect in the conical spin structure with 89% efficiency. The numerical parameters used in our calculations are summarized in Table 1.

1. Fraunhofer patterns for a single and double vortex configurations

Fig. A1 shows Fraunhofer patterns for a single vortex (a) antivortex (b) located at $(x_v, y_v)/L_y = (0.01, 0.1)$. The case of double vortex (c) antivortex (d) located at $(x_{v_1}, y_{v_1})/L_y = (0.05, 0.1)$, $(x_{v_2}, y_{v_2})/L_y = (0.05, -0.1)$ shows a greater shift of the maximum supercurrent compared to the single vortex case, which qualitatively match the experimental magnetic diffraction patterns.

Parameter	Symbol	Value
Number of lattice sites in the \hat{x} direction	N_x	7
Number of lattice sites in the \hat{z} direction	N_z	11
Hopping parameter	t	1
Exchange interaction strength	Δ_c	0.001
Polar angle for spin orientation	θ	60° or 90°
Azimuthal angle for spin orientation	ϕ	9°
Superconducting order parameter at the contacts	$\Delta_{L(R)}$	0.1
Transmission Coefficient of contacts	$\tau_{L(R)}$	0.01
Small positive value to avoid singularity	η	0.0001
Energy	ϵ	-0.0024
Superconducting phase at left contact	ϕ_L	0°
Superconducting phase at right contact	ϕ_R	from 0° to 360°

Table A1. Numerical Parameters Used in the Calculations